

Soap bubbles for large-scale PIV in industrial wind tunnels

David Engler Faleiros^{1,3,*}, Marthijn Tuinstra¹,
Bart D. van Rooijen²
Fulvio Scarano³, Andrea Sciacchitano³

¹ Helicopters and Aeroacoustics Department, Netherlands Aerospace Centre (NLR), the Netherlands

² German-Dutch Wind Tunnels (DNW), the Netherlands

³ Faculty of Aerospace Engineering, Delft University of Technology, the Netherlands

*david.engler.faleiros@nlr.nl

Abstract

This work evaluates the use of helium-filled soap bubbles (HFSB) for Particle Image Velocimetry (PIV) measurements at high Reynolds numbers (up to 3.2 million) in aeronautics. The measurements are performed in the Low Speed Tunnel (LST) of the German-Dutch Wind Tunnels (DNW) using a high-lift airfoil in close-to-stall conditions up to 70 m/s. Experiments using Di-ethyl-hexyl-sebacat (DEHS) particles are performed for a comparison of the two seeding techniques. The signal to noise ratio of HFSB images was two orders of magnitude larger than that of DEHS, which strongly reduced the unwanted effects of background reflections and light intensity spatial variations, compared to DEHS particle images. The mean velocity field obtained with HFSB exhibits differences typically within 1% of the free stream velocity, when compared to DEHS measurements.

1. Introduction

Conventional particles used for Particle Image Velocimetry (PIV) in air (e.g. fog or di-ethyl-hexyl-sebacat, DEHS) are typically much denser (10^3 kg/m^3) than the medium. The mismatch in density potentially introduces a lag in the velocity of particles with respect to the fluid velocity (Adrian and Westerweel, 2011), which is minimized by using small particles (1 to 2 μm diameter). However, such approach is optically ineffective, because the energy of the scattered light by particles larger than the wavelength of the incident light is proportional to their cross-sectional area (Adrian and Westerweel, 2011), limiting the size of the observable region for a given laser power. Usually, micron-sized particles cannot be used for large-scale PIV (i.e. measurement area $> 1 \text{ m}^2$) as the signal to noise ratio (SNR) becomes insufficient. For volumetric measurements in wind tunnels, the measurement domain achieved with microparticles as tracers is further restricted as it seldom exceeds 100 cm^3 (Scarano et al. 2015).

Particles approaching the neutral buoyancy point (density approaching that of the medium) can react within short time. In the Stokes flow regime, the response approaches zero, for neutrally buoyant tracers (Raffel et al. 2018). Therefore, a certain degree of relaxation in the particle size is allowed as far as their density is close to that of the airflow. The use of sub-millimeter ($\sim 0.5 \text{ mm}$ diameter) neutrally buoyant helium-filled soap bubbles (HFSB) as tracers is reported to increase the amount of reflected light by 10^4 - 10^5 (Caridi, 2018), which allows increasing the measurement volume by approximately two orders of magnitude (Scarano et al. 2015). As a result, large-scale PIV becomes possible in wind tunnels without the use of systems often involving multiple lasers and traversing mechanisms (e.g. de Gregorio et al. 2010). The reduction of complexity of setting up large-scale PIV systems is a crucial step for the deployment of PIV measurements in industrial facilities, where large observation areas are required and the operational costs of wind tunnels are high.

The use of HFSB for quantitative measurements in wind tunnels has not been extensive prior to this decade due to the technical complexity of realizing systems that produce neutrally buoyant bubbles under controlled conditions and in large amounts (e.g. Kerho and Bragg, 1994). The development of miniaturized bubble generators (Bosbach et al. 2009), based on the design of Okuno et al. (1993), facilitated the controlled production of HFSB. Investigations on the generation of neutrally-buoyant helium-filled soap bubbles in a controlled manner are now available in the literature (Morias et al. 2016, Gibeau et al. 2018 and Faleiros et al. 2019).

The tracing fidelity of HFSB has been verified in the past few years along the stagnation streamline in front of a cylinder (Scarano et al. 2015) as well as in boundary layer turbulence (Faleiros et al. 2018). The results have shown small differences for neutrally-buoyant bubbles (mean slip velocities of approximately 2%) in comparison to more established tracing particles. Still, achieving particle concentration levels that are useful for wind tunnel measurements required further developments of systems that operate simultaneously a multitude of generators (Caridi et al. 2016).

The latter studies are encouraging; however, there has not been yet an evaluation of the measurement accuracy of PIV using HFSB as tracers in conditions closer to that normally applied by the aeronautical industry. Recently, large-scale PIV using HFSB has been applied to a 1:12 scaled version of the EADS CASA C-295 aircraft (Sciacchitano et al. 2018) in the Low-Speed Tunnel (LST) of the German-Dutch Wind Tunnels (DNW). Still, the study has not provided an assessment of the measurement errors or a comparison with other established measurement techniques.

In this study, PIV measurements using HFSB were set up and performed in the LST of the German-Dutch Wind Tunnels over the suction side of a high-lift airfoil at incidence reaching near stall conditions. The experiments were performed at Reynolds number up to 3.2 million. The measurements with HFSB are compared to state-of-the-art planar PIV measurements using micron-size (DEHS) particles to understand the limits of the former technique in this experimental regime. The accuracy of the ensemble average of individual particles velocity obtained using HFSB is established for the purpose of advancing aerodynamic measurements techniques in industrial wind tunnels.

2. Setup of experiment and data acquisition

The experiments were conducted in the Low-Speed Tunnel (LST) of the German-Dutch Wind Tunnels (DNW) in the Netherlands. The LST is a closed-circuit tunnel with a closed-test section of 3 m (height) \times 2.25 m (width) cross-section, with an area contraction rate of 9 and low free-stream turbulence level ($\sim 0.03\%$). A high-lift airfoil of 69.2 cm chord (flap included) was installed vertically spanning the full test section height. The flap angle was kept at zero degrees during the tests. The measurements were performed at 15, 40 and 70 m/s free stream velocities and at three angles of attack $\alpha = [9^\circ, 14^\circ, 17^\circ]$.

The 2D2C-PIV system (Figure 1) features two LaVision *Imager* sCMOS cameras (2560×2160 px², 16 bit, 6.5 μm pixel pitch) equipped with 50 mm focal length objectives (lens aperture diameter of $f/16$ for HFSB and $f/5.6$ for DEHS). The cameras were installed on the top of the test section and attached to the turntable so that different angles of attack could be realized using the same optical calibration. As a result, the coordinate axes refer to the airfoil system of reference. The cameras were placed perpendicular to the laser sheet at about 1.5 meters above it and 47.5 cm apart from each other. The camera imaging resolution is of 0.2 mm/px (optical magnification is 0.03), rendering a FoV of 0.5×0.42 m² per camera. With the FoV of both cameras overlapping in 2 cm in the chordwise direction, the combined FoV is 0.95×0.4 m², covering the whole chord of the airfoil.

A Quantel *Evergreen 200* Nd:YAG laser (2x200 mJ/pulse at 15 Hz) was used for particle illumination. The illuminated plane was at 1 meter span position from the test section floor. The laser sheet thickness was 10 mm for HFSB and about 4 mm for DEHS. The laser power was set at 40% for the former and 100% for the latter.

The acquisition was performed in straddling mode (double frame, single exposure) for both HFSB and DEHS. The laser repetition rate limited the acquisition frequency to 15 Hz. The time interval between the two laser pulses was defined depending on the wind tunnel speed and particle concentration, varying from 30 to 105 μ s (free stream displacement from 1.5 to 2 mm). The acquisition and optical imaging conditions are summarized in Table 1 and Table 2.

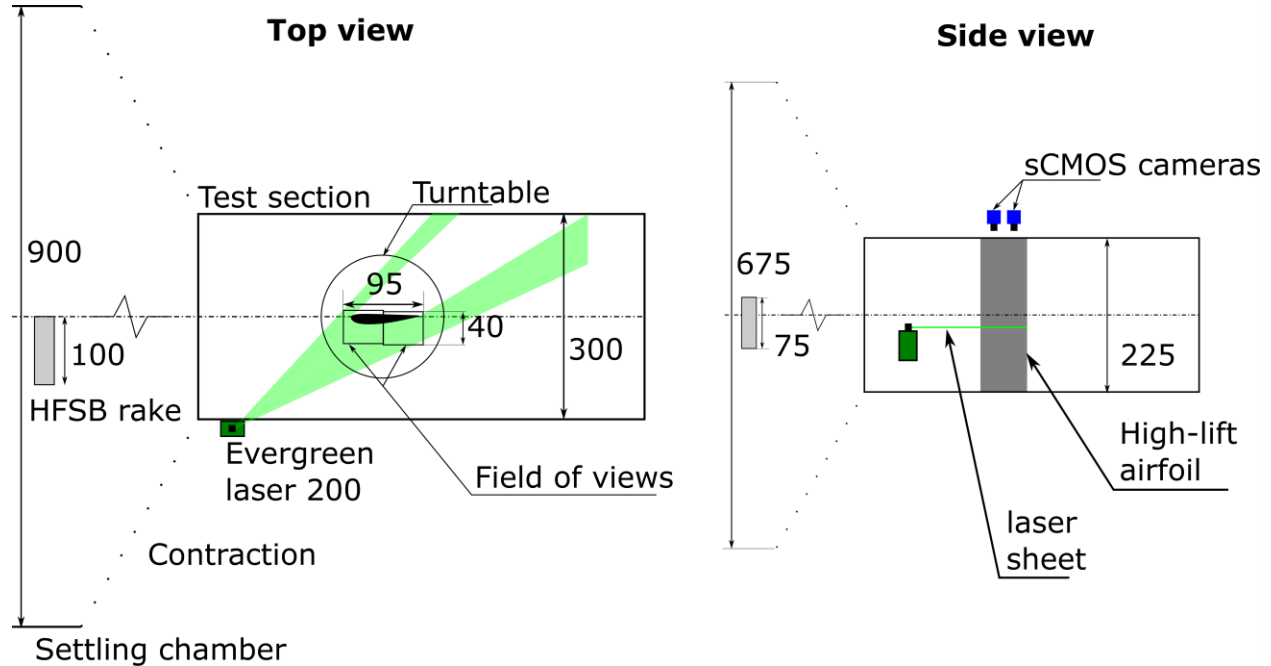


Figure 1. Experimental Setup. The wind tunnel area contraction (1:9) is represented by dotted lines. The dimensions are given in centimeters.

α	U_∞ (m/s)	Re (10^6)	Pulse separation (μ s)	N° images HFSB	N° images DEHS
9°	15	0.7	105	2,000	2,000
	40	1.8	45	5,500	6,000
	70	3.2	30	9,500	1,000
14°	15	0.7	105	10,000	5,000
	40	1.8	45	27,000	5,000
	70	3.2	30	20,000	2,000
17°	15	0.7	105	10,000	5,000
	40	1.8	45	27,000	5,000
	70	3.2	30	37,000	3,000

Table 1. Test matrix

Seeding	DEHS	HFSB
Cameras sensor size	2560 × 2160 px ²	2560 × 2160 px ²
Cameras objective focal length	50 mm	50 mm
Combined field of view	0.95 × 0.40 m ²	0.95 × 0.40 m ²
Image resolution	0.2 mm/px	0.2 mm/px
Lens aperture diameter	f/5.6	f/16
Laser sheet thickness	4 mm	10 mm
Acquisition frequency	15 Hz	15 Hz
Laser pulse energy	200 mJ	80 mJ

Table 2. Imaging conditions

2.1. HFSB generation

The system of HFSB generation is composed of three main components: the fluid supply unit (FSU), the bubble generators and the seeding rake. The in-house built FSU is composed of vessels and valves that can be operated remotely to pressurize and depressurize the fluid supply lines. Pressure flow controllers (coupled with mass flow meters) from Bronkhorst control the flow rates of helium, soap and air. The bubble generators are CNC-manufactured nozzles of 1 mm orifice diameter (Faleiros et al. 2019) designed by the Netherlands Aerospace Centre (NLR). Flow resistors guarantee equal mass flow to each bubble generator. The seeding rake is a 42-generator array composed of six horizontal segments spaced vertically by 15 cm (Figure 2). Each segment contains seven bubble generators spaced with a 15 cm pitch. The bubble system, therefore, provides a seeded stream tube of about of 0.75 m (height) \times 0.90 m (width) cross-section area, with an injection rate of approximately 1.3 million bubbles/s. With the seeding rake installed in the settling chamber, the resultant stream tube of HFSB after contraction is 0.25 m (height) \times 0.30 m (width). The bubble generator dimensions, working principle, regimes of generation and bubble properties have been recently studied by the authors (Faleiros et al. 2019). In the present experiments the average volume flow rates per generator were 80 l/h of air, 9.5 l/h of helium and 9.5 l/h of soap, yielding 30,000 bubbles/s (per generator) of nominal bubble density of 1.1 kg/m³ and mean diameter of 0.5 mm.

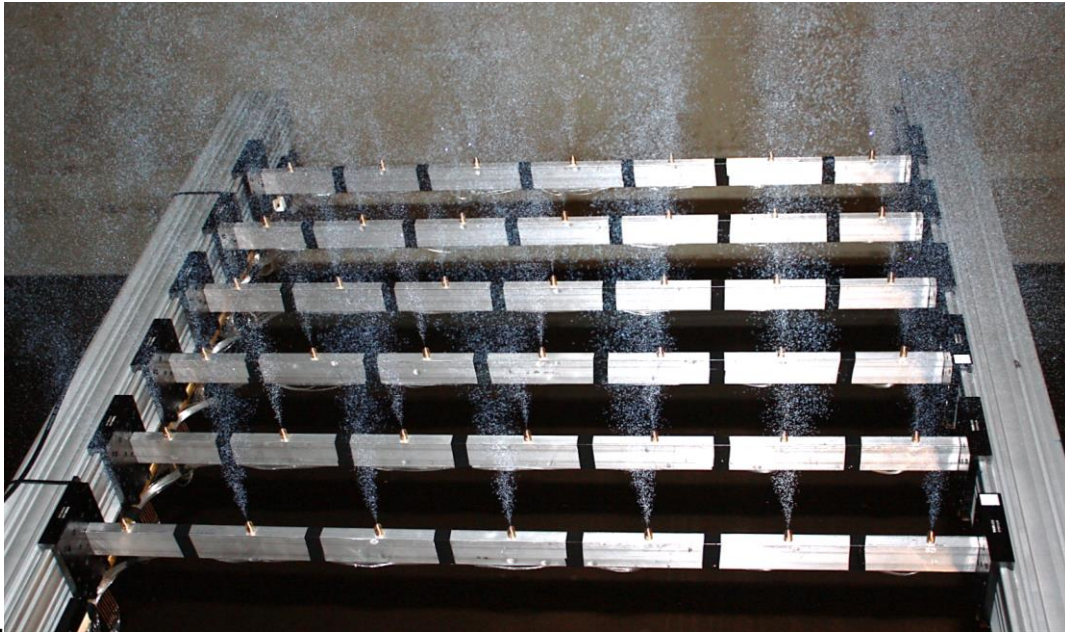


Figure 2. NLR's HFSB 42-bubble generators seeding rake.

2.2. Data processing

The data obtained using DEHS was processed using the cross-correlation algorithm from the LaVision software *DaVis 10*. The final interrogation window used was of 48 \times 48 pixels (0.96 cm \times 0.96 cm in physical space). With an overlap of 75% among adjacent interrogation windows, the vector spacing is 0.24 cm. The data acquired with HFSB was processed using an algorithm developed in-house with Matlab. Particles were identified based on local maxima and paired to the particles in the next frame according to the nearest neighbor criterion. The particle displacement in this case was sufficiently small compared to the average particle distance. After velocity vectors were obtained, the FoV were divided into bins of 1.2 cm (width) \times 1 cm (height) for statistical analysis.

3. Data quality

Inspection of the raw images elucidates one of the advantages of using HFSB: the high signal to noise ratio. The raw data without any pre-processing is shown for HFSB and DEHS in Figure 3. The image background intensity is approximately 300 counts in this experiment, which is due to reflections of laser light within the test section. The signal from DEHS particles barely overcomes the noise level, reaching an SNR of about 1.5 (Figure 4). The HFSB signal reaches over 30,000 counts with SNR > 100. Not only the background noise becomes negligible compared to the signal from HFSB particles, but also the localized laser reflections onto the airfoil model are somewhat less bright than the bubbles peak intensity. Furthermore, it is noted that the laser light is at its full capacity (200 mJ per pulse) for the DEHS case, while only a fraction of it is needed for imaging of HFSB, even at lens aperture of $f/16$, compared to $f/5.6$ for DEHS.

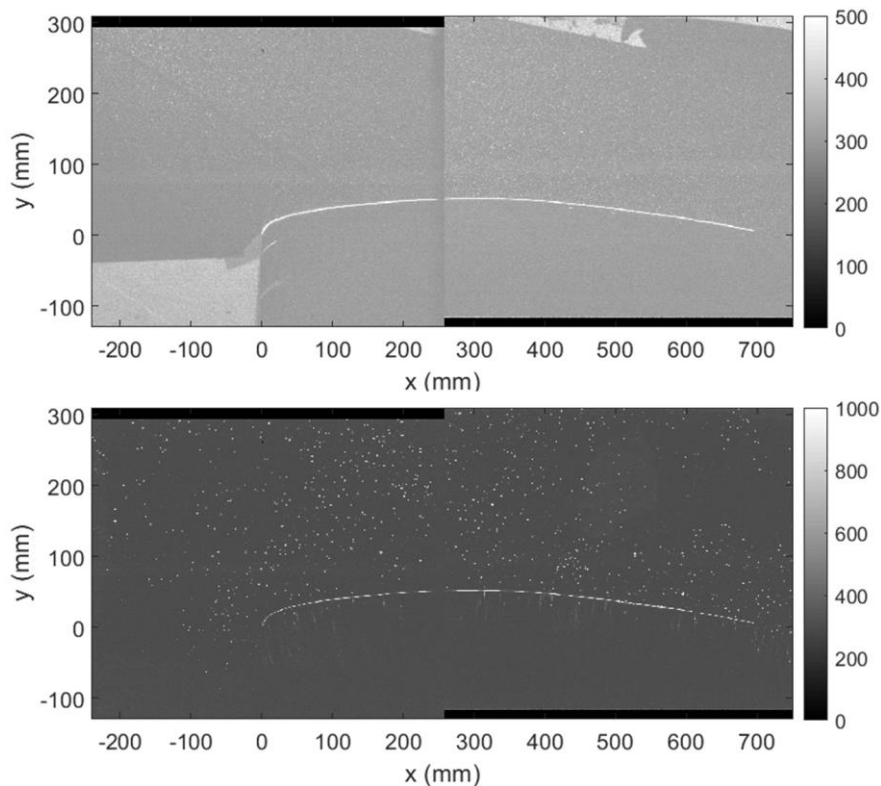


Figure 3. Raw images DEHS (top) and HFSB (bottom).

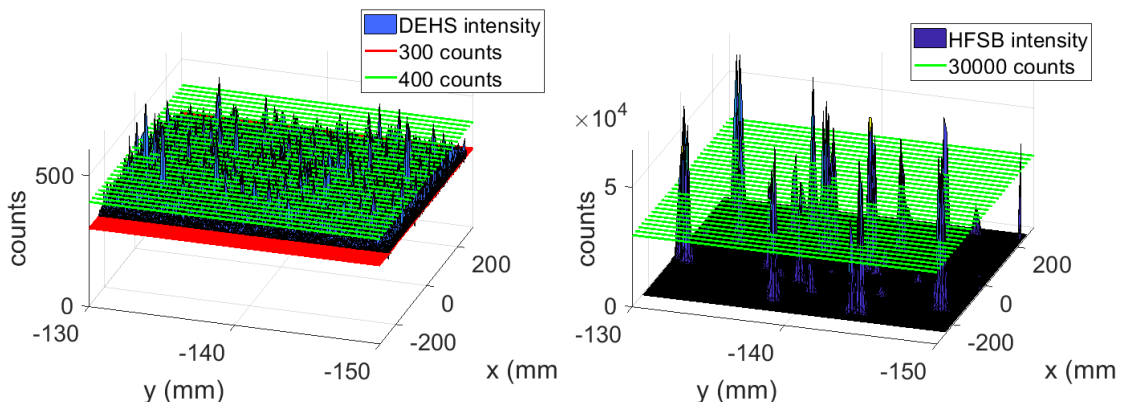


Figure 4. Particle signal vs. noise level for DEHS (left) and HFSB (right). The noise level is about 300 counts for both particles. The signal to noise ratio is about 1.5 for DEHS and more than 100 for HFSB.

4. HFSB concentration

The concentration of HFSB for this seeding rake design and measurement conditions is typical of PTV measurements. The number of particles is too low to perform spatial correlation analysis of the instantaneous images (PIV uses typically 5-10 particles per interrogation window). Moreover, the concentration of HFSB decreases with increasing velocity: the bubble concentration is about 5 times larger at 15 m/s than at 70 m/s, which needs to be compensated at higher velocity by increasing the number of images acquired for the experiment (see Table 1). When the latter effect is taken into account, similar amount of vectors per bin (1.2 cm^2) can be obtained irrespective of the flow speed. The number of tracked particles per bin for 15 m/s and 70 m/s at 9° incidence is shown in Figure 5. The number of detected vector samples exhibits some spatial variation, with more samples detected in the upper region and less approaching the airfoil. Such variation is ascribed to the distribution of laser light intensity. The number of vectors per bin being one-fourth to one-tenth of the total number of images demands more images to be acquired for similar statistical convergence as DEHS (Table 1). Furthermore, the decay in the number of vectors where the fields of view overlap ($x = 250 \text{ mm}$) is due to signal drop in the edge of the upstream field of view.

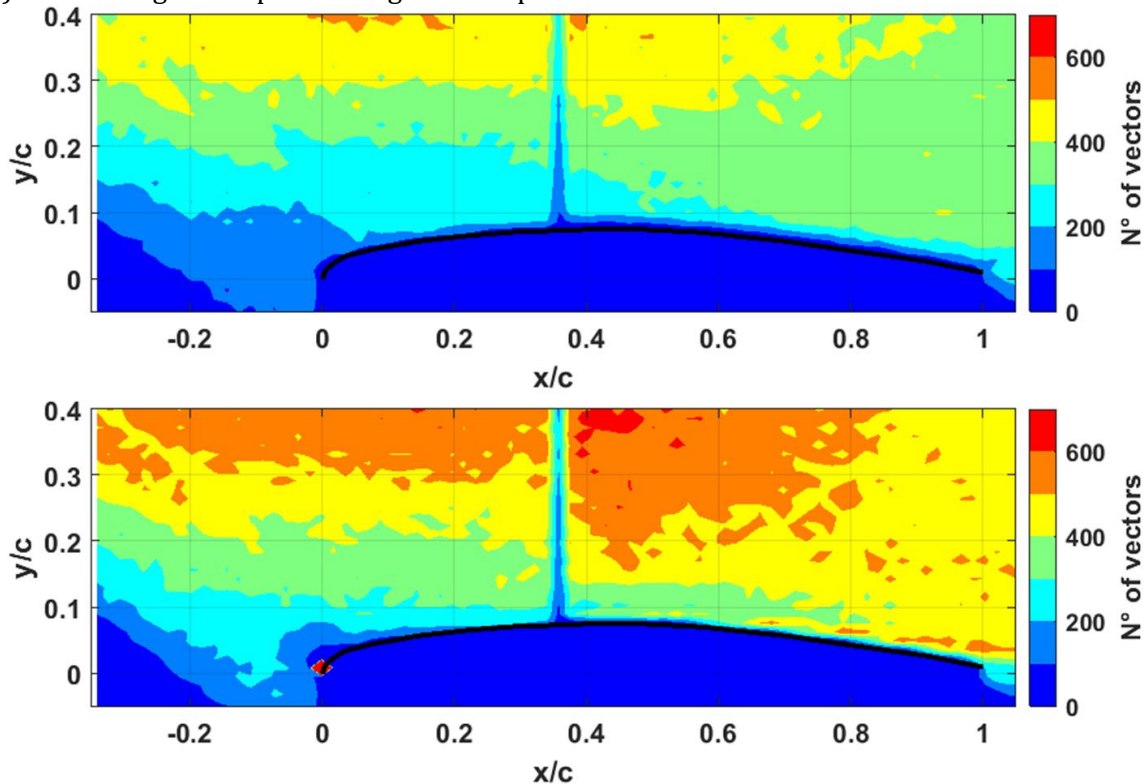


Figure 5. HFSB concentration at 15 m/s (top) and 70 m/s (bottom) and at 9° incidence for $N = 2000$ images and $N = 9500$ images, respectively. Bin size of 1.2 cm (width) \times 1.0 cm (height).

5. Mean velocity

The normalized mean velocities U/U_∞ and U_b/U_∞ (subscript b for “bubbles”) at 70 m/s free stream velocity and 9° incidence is shown in Figure 6 for DEHS (top) and HFSB (bottom), respectively. The color contours indicate a good agreement between the measurements obtained with different tracer particles. In the front region of the airfoil, laser light impinging almost normally, introduce intense light reflections corrupting the data obtained with DEHS to a larger extent than for the HFSB. A more restrictive mask is applied for DEHS data and vectors with correlation lower than 0.15 are discarded. This is also the case near the airfoil surface, requiring the mask used in the DEHS processing to be shifted further away from the surface than in the HFSB case.

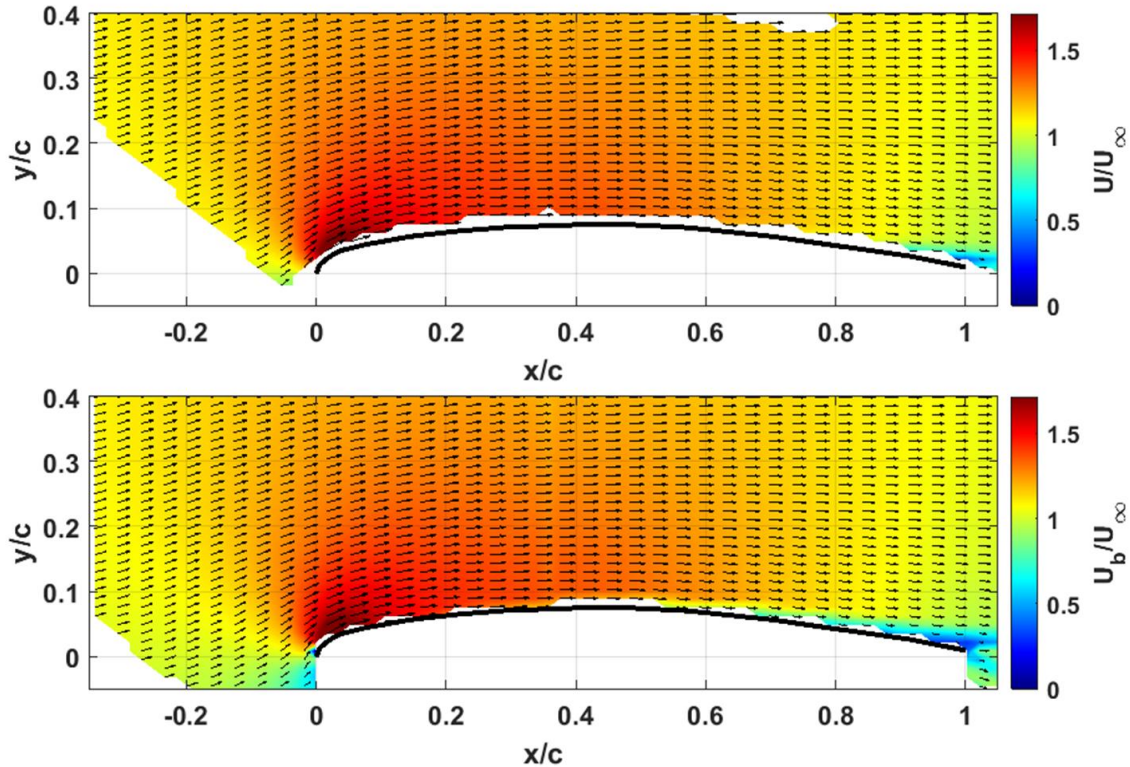


Figure 6. Velocity magnitude of DEHS (top) and HFSB (bottom) at $U_\infty = 70$ m/s and $\alpha = 9^\circ$

Isolines of the normalized velocity components in chordwise u/U_∞ and normal to chord directions v/U_∞ from HFSB (color plots and dashed lines) and DEHS (solid lines) are plotted against each other (Figure 7 to Figure 9) for ease of comparison. Three measurement conditions are presented in the discussion for sake of conciseness: 15 m/s and 70 m/s at $\alpha = 9^\circ$ and 70 m/s at $\alpha = 17^\circ$. The isolines of the mean velocity obtained with HFSB and DEHS are in significant agreement for both velocity components. Only in some cases a more pronounced difference is observed (see for instance the isoline $v_b/U_\infty = 0.3$ upstream of the model in Figure 7, bottom). Overall, the discrepancies among DEHS and HFSB stay in the order of $0.01 U_\infty$.

Furthermore, the local differences in mean velocity $\Delta u = |u - u_b|$ and $\Delta v = |v - v_b|$ can be appreciated through analysis of velocity profiles at certain x/c locations: 0.04, 0.79 and 0.98. At 15 m/s free stream velocity and 9° incidence (Figure 10) Δu is up to $\sim 1\%$ of U_∞ for $y/c > 0.15$. The deviations increase closer to the airfoil surface, reaching 10% of U_∞ for $y/c < 0.05$ in the trailing edge region. The normal velocity component deviates less than 1% of U_∞ , with exception of the region close to the surface in proximity of the leading edge ($x/c = 0.04$, $y/c = 0.05$), where Δv reaches $\sim 5\%$ of U_∞ . At $U_\infty = 70$ m/s and same incidence (Figure 11), the differences are similar to the case of lower velocity. For $y/c > 0.15$, both components of velocity deviate less than 1%. Close to the surface ($y/c < 0.1$), the differences are more pronounced with Δu reaching 3% of U_∞ at $x/c = 0.04$ and 20% for $x/c = 0.79$ and $x/c = 0.98$. Deviations in the normal component are mostly smaller than 1%, increasing in proximity to the surface ($y/c < 0.15$). The latter is observed to increase exponentially at $x/c = 0.04$ as y/c decreases, reaching approximately 10%. At 70 m/s free stream velocity and $\alpha = 17^\circ$ (Figure 12), the deviations are comparable to the case of lower incidence ($\alpha = 9^\circ$).

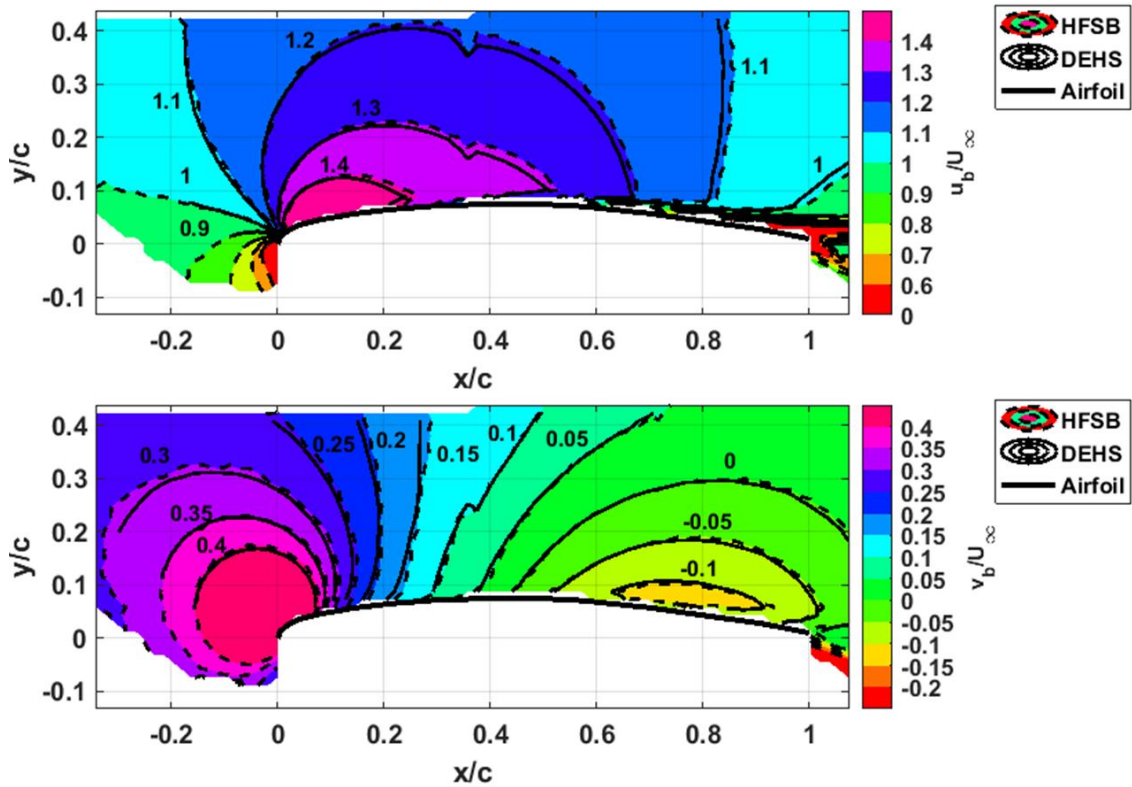


Figure 7. Velocity contours of chordwise (top) and normal to chord (bottom) components at $U_\infty = 15$ m/s and $\alpha = 9^\circ$

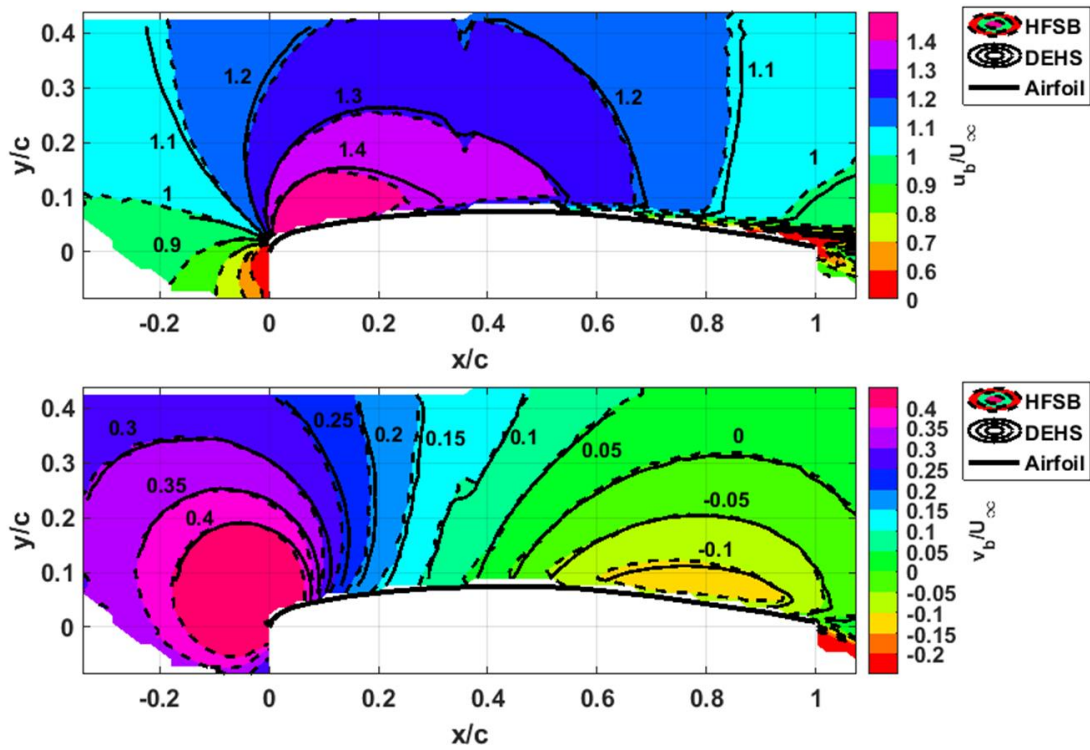


Figure 8. Velocity contours of chordwise (top) and normal to chord (bottom) components at $U_\infty = 70$ m/s and $\alpha = 9^\circ$

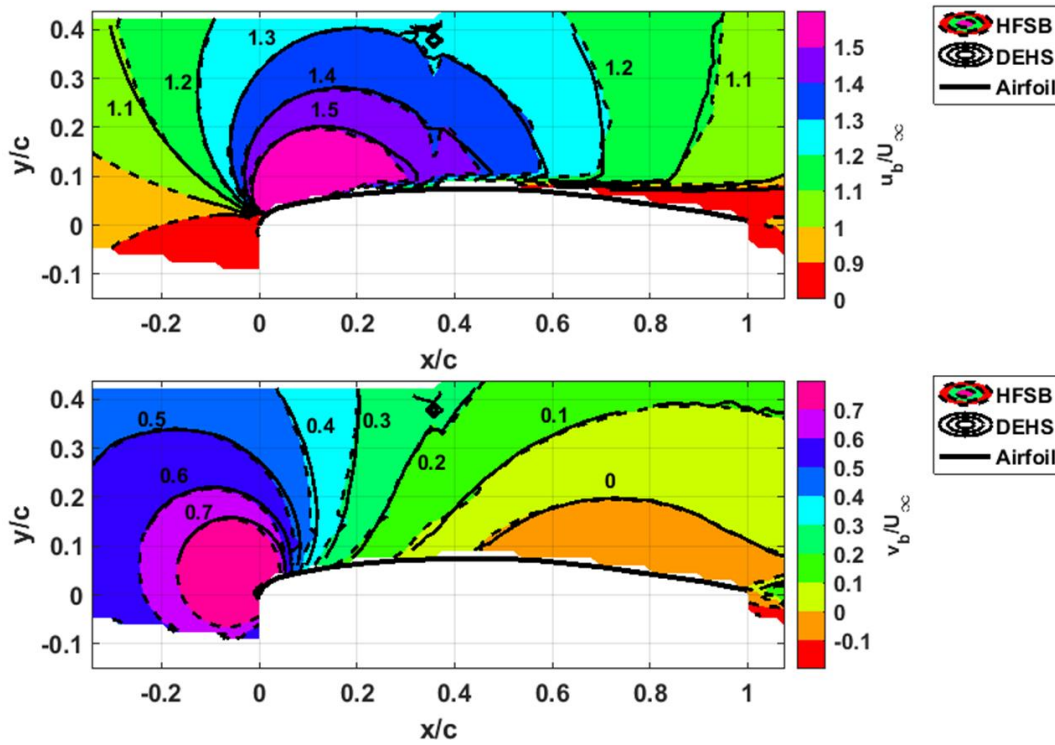


Figure 9. Velocity contours of chordwise (top) and normal to chord (bottom) components at $U_\infty = 70$ m/s and $\alpha = 17^\circ$

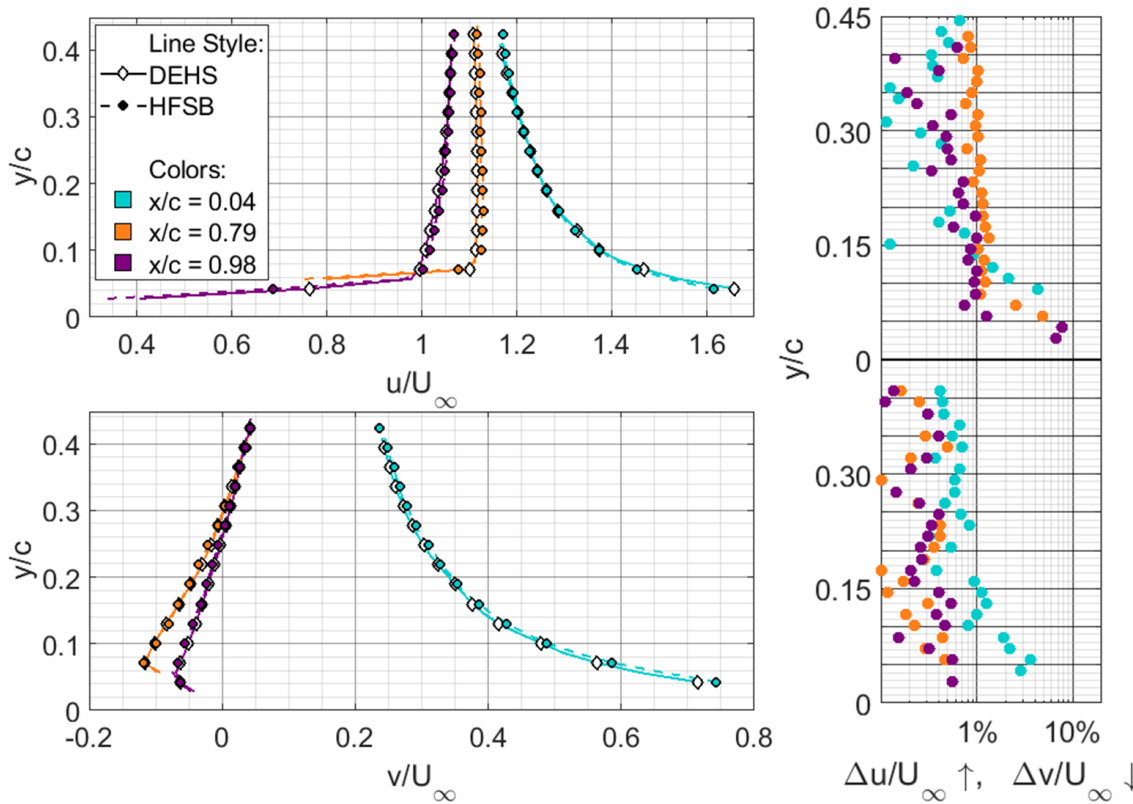


Figure 10. Chordwise (top, left) and normal to chord (bottom, left) velocity components at $U_\infty = 15$ m/s and $\alpha = 9^\circ$ (one marker every two points), and absolute velocity differences (right).

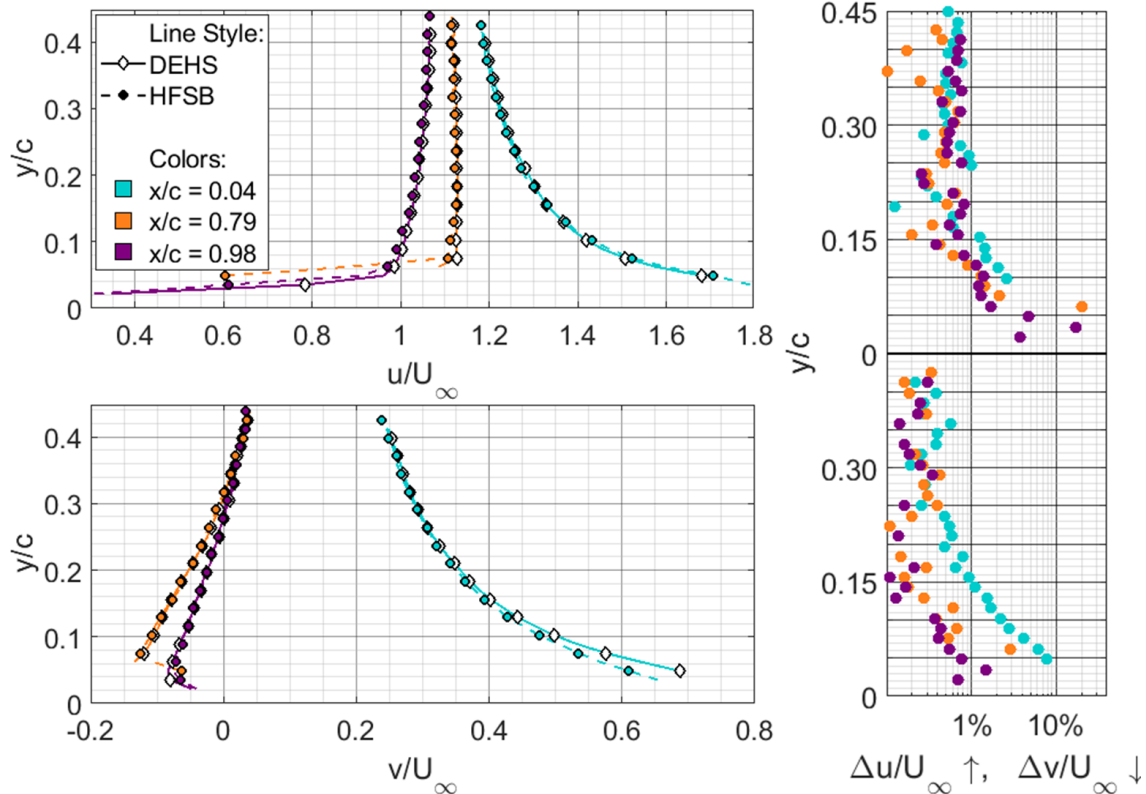


Figure 11. Chordwise (top, left) and normal to chord (bottom, left) velocity components at $U_\infty = 70$ m/s and $\alpha = 9^\circ$ (one marker every two points), and absolute velocity differences (right).

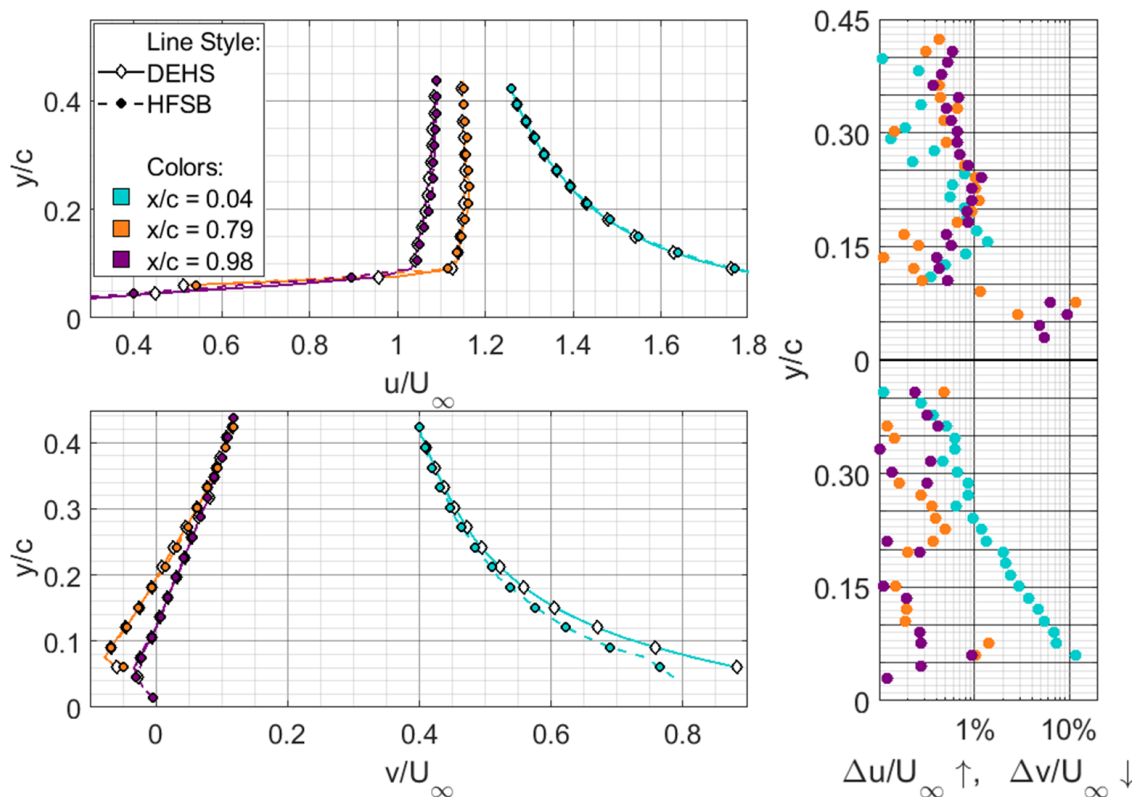


Figure 12. Chordwise (top, left) and normal to chord (bottom, left) velocity components at $U_\infty = 70$ m/s and $\alpha = 17^\circ$ (one marker every two points), and absolute velocity differences (right).

6. Conclusions

Measurements performed at high Reynolds numbers up to 3.2 million and large incidence from 9° to 17° with a seeding rake of helium-filled soap bubbles (42 bubble generators) showed a convincing agreement with the reference DEHS, with deviations of mean velocity up to 1% U_∞ in most cases. The largest differences observed near the airfoil surface, where the lower quality of the reference data could lead to misleading interpretations. A distinct deviation was observed only in proximity to the leading edge region at 70 m/s that in the normal component of velocity, which reached 10% of U_∞ for $y/c < 0.1$.

The SNR of HFSB is two orders of magnitude larger than that of DEHS, significantly improving the quality of the data, where reflections overwhelm the particle signal of conventional seeding. Furthermore, if the field of view were to be enlarged, DEHS would be unfit for the measurement, while in the HFSB case, the laser pulse energy was limited to 40% and the lens aperture was fully closed ($f/16$).

The low concentration of HFSB slows down statistical convergence of the data, requiring (for the cases here tested) four to ten times more images to be acquired for a similar convergence as DEHS.

7. References

- Adrian RJ, Westerweel J (2011) Particle image velocimetry. Cambridge University Press, New York
- Bosbach J, Kühn M, Wagner C (2009) Large scale particle image velocimetry with helium filled soap bubbles. *Exp Fluids* 46:539
- Caridi GCA, Ragni D, Sciacchitano A, Scarano F (2016) HFSB seeding for large scale tomographic PIV in wind tunnels. *Exp Fluids* 57:190
- Caridi GCA (2018) Development and application of helium-filled soap bubbles for large-scale PIV experiments in aerodynamics, PhD Thesis.
- de Gregorio F, Pengel K, and Kindler K (2010) Industrial measurement campaign on fully equipped helicopter model. 15th International symposium on applications of laser techniques to fluid mechanics, Lisbon
- Faleiros DE, Tuinstra M, Sciacchitano A, Scarano F (2018) Helium-filled soap bubbles tracing fidelity in wall-bounded turbulence. *Exp Fluids* 59:56
- Faleiros DE, Tuinstra M, Sciacchitano A and Scarano F (2019) Generation and control of helium-filled soap bubbles for PIV, *Exp in Fluids* 60:40
- Gibeau B, Ghaemi S (2018) A modular, 3D-printed helium-filled soap bubble generator for large-scale volumetric flow measurements. *Exp Fluids* 59:12
- Morias KLL, Caridi GCA, Sciacchitano A, Scarano F (2016) Statistical characterization of helium-filled soap bubbles tracing fidelity for PIV. 18th International symposium on the application of laser and imaging techniques to fluid mechanics, Lisbon
- Okuno Y, Fukuda T, Miwate Y, Kobayashi T (1993) Development of three dimensional air flow measuring method using soap bubbles. *JSAE Rev* 14(4):50–55
- Raffel M, Willert CE, Scarano F, Kähler C, Wereley ST, Kompenhans J (2018) Particle image velocimetry—a practical guide, 3rd edn. Springer, Berlin
- Scarano F, Ghaemi S, Caridi GCA, Bosbach J, Dierksheide U, Sciacchitano A (2015) On the use of helium filled soap bubbles for large scale tomographic PIV in wind tunnel experiments. *Exp Fluids* 56:42
- Sciacchitano A, Giaquinta D, Schneiders JFG, Scarano F, van Rooijen BD, and Funes DE (2018) Quantitative Flow Visualization of a Turboprop Aircraft by Robotic Volumetric Velocimetry. In Proceedings 18th International Symposium on Flow Visualization, ETH Zurich